PAPER • OPEN ACCESS

An x-ray regenerative amplifier free-electron laser using diamond pinhole mirrors

New Journal of Physics

The open access journal at the forefront of physics

CrossMark

OPEN ACCESS

PAPER

An x-ray regenerative amplifier free-electron laser using diamond pinhole mirrors

H P Freund[1,2], P J M van der Slot[3] and Yu Shvyd'ko[4]

1　Department of Electrical and Computer Engineering, University of New Mexico, Albuquerque, NM, United States of America
2　Calabazas Creek Research, San Mateo, CA, United States of America
3　Mesa+ Institute for Nanotechnology, University of Twente, Enschede, The Netherlands
4　Advanced Photon Source, Argonne National Laboratory, Argonne, IL, United States of America

E-mail: p.j.m.vanderslot@utwente.nl

Keywords: oscillator, regenerative amplifier, x-ray, free-electron laser

Abstract

X-ray free-electron lasers (FELs) rely on SASE due to the lack of seed lasers and the difficulty in obtaining mirrors. Progress in diamond crystal Bragg mirrors enables the design of x-ray FEL oscillators. Regenerative amplifiers (RAFELs) are high gain/low-Q oscillators that out-couple most of the optical power. An x-ray RAFEL based on the LCLS-II at SLAC using a six-mirror resonator out-coupling 90% or more through a pinhole in the first downstream mirror is analyzed using the MINERVA simulation in the undulator and OPC for the resonator. Results show substantial powers at the fundamental (3.05 keV) and 3rd harmonic (9.15 keV).

1. Introduction

Development of x-ray free electron lasers (XFELs) began in the United States with the proposal for the Linac Coherent Light Source (LCLS) at the Stanford Linear Accelerator Center (SLAC) culminating with first lasing in 2009 [1]. The success of the LCLS encouraged the development of other XFELs worldwide [2–4]. Due to the lack of seed lasers at x-ray wavelengths, however, each of these facilities rely upon self-amplified spontaneous emission (SASE) in which the optical field grows from electron shot noise to saturation in a single pass through a long undulator. While pulse energies of the order of 2 milliJoules have been achieved at Ångstrom to sub-Ångstrom wavelengths, SASE exhibits shot-to-shot fluctuations in the output spectra and power of about 10%–20%. For many applications, these fluctuations are undesirable, and efforts are underway to find alternatives, including, amongst others, self-seeding [5, 6], which improves the temporal coherence at the expense of larger pulse-to-pulse energy fluctuations.

The utility of an x-ray FEL oscillator (XFELO) has been under study for a decade [7–14] making use of resonators based upon Bragg scattering from high-reflectivity diamond crystals [15–19]. The development of these crystals is a major breakthrough in the path toward an XFELO. Estimates indicate that using a superconducting rf linac producing 8 GeV electrons at a 1 MHz repetition rate is capable of producing 10^{10} photons per pulse at a 0.86 Å wavelength with a FWHM bandwidth of about 2.1×10^{-7}. This design is consistent with the LCLS-II high energy upgrade [20]. As a consequence, an XFELO on a facility such as the LCLS-II and LCLS-II-HE is expected to result in a decrease in SASE fluctuations in the power and spectrum and to narrow the spectral linewidth.

As with the majority of FELOs to date [21–23], the aforementioned XFELOs use low gain/high-Q resonators with transmissive out-coupling through thin diamond crystals [14]. Potential difficulties with low-gain/high-Q resonators derive from sensitivities to electron beam characteristics and mirror loading and alignments. While experiments show that diamond crystals can sustain relatively high thermal and radiation loads [17, 24], transmissive out-coupling cannot be easily achieved at the photon energies of interest here. Hence, we consider an XFELO design with high out-coupling efficiency using a pinhole diamond mirror based on a regenerative amplifier (RAFEL) [25, 26].

The RAFEL is based on a high-gain/low-Q resonator where the majority of the power is out-coupled on each pass [27]. Typically, this ranges from 90% to 95% of the power. Hence, the mirror loading is significantly

reduced relative to that in a high-Q resonator. Since the interaction in a RAFEL optically guides the light, the optical mode is characterized by high purity with $M^2 \approx 1$ whether hole or transmissive out-coupling is used [28]. This might include an unstable resonator; however, it was shown by Siegman [29] that gain guiding, such as in an free-electron laser (FEL), will stabilize a resonator that is otherwise (i.e. *in vacuo*) unstable.

The properties of a RAFEL are similar to SASE FELs in some ways [28, 29]. Since a RAFEL employs a high-gain undulator, peak gain is found on-resonance, and the Pierce parameter, ρ, determines the efficiency ($\eta \approx \rho$) and spectral linewidth ($\Delta\omega/\omega \approx \rho$), assuming no additional spectral filtering within the resonator. In contrast to low-gain oscillators where the mode structure is governed largely by the resonator, there is strong optical guiding within the undulator in a RAFEL and this is an important factor controlling the transverse mode structure. It should be noted that low-gain oscillators at long wavelengths where short undulators may be used often exhibit higher efficiencies than either FEL amplifiers or SASE FELs because the efficiency scales as $\eta \approx 1/2N_w$ [30] and this is often higher than the Pierce parameter. However, a low-gain XFELO would require a long undulator and the efficiency would likely be no higher than that of a RAFEL. As in a low-gain XFELO, the RAFEL will improve the temporal coherence with respect to SASE due to multiple passes of the optical field through the resonator.

In this paper, we analyze an x-ray RAFEL based upon a six-mirror resonator composed of diamond crystal Bragg reflectors. High-efficiency out-coupling is achieved through a pinhole in one of the diamond crystals. We consider that the resonator is implemented on the LCLS-II beamline at SLAC using the HXR (i.e. high energy x-ray) undulator and produces x-ray photons at energies of 3.05 keV in the fundamental and 9.15 keV at the 3rd harmonic. Simulations are conducted using the MINERVA simulation code [31, 32] for the undulator interaction and the optics propagation code (OPC) to describe the propagation of the x-rays through the resonator [33, 34].

OPC was modified to treat reflections from the diamond crystal Bragg mirrors where the mirror losses and angles of reflection depend on the crystal orientation/geometry, the x-ray energy and wavelength. X-ray Bragg mirrors typically have a very narrow reflection bandwidth and a narrow angle of acceptance [35]. To handle this, OPC first calculates a temporal Fourier transform. For the RAFEL, and for computational efficiency, this is done once at the beginning of the optical path when the optical field is passed from MINERVA to OPC and the propagation is performed in the wavelength domain, i.e. each wavelength is independently propagated through the resonator. An inverse Fourier transform is calculated at the end of the optical path, before the field is handed back to MINERVA. As the optical field inside the cavity is typically not collimated, a spatial Fourier transform in the transverse coordinates is calculated for each of the wavelengths when a Bragg mirror is encountered. Each combination of transverse and longitudinal wavenumber corresponds to a certain photon energy and angle of incidence on the Bragg mirror and these parameters are used to calculate the complex reflection and transmission coefficients of the Bragg mirror [35]. After applying the appropriate parameter to the optical field, depending on whether it is reflected or transmitted, the inverse spatial Fourier transform is calculated and the field is propagated to the next optical element along the path until the end is reached.

MINERVA/OPC has been validated by comparison with the 10 kW Upgrade experiment at Jefferson Laboratory [31, 36] and has also been used to simulate a RAFEL with a ring resonator [28]. Hence, MINERVA/OPC is capable of simulating FELOs at wavelengths from the infrared through the x-ray spectra.

2. The diamond crystal resonator

We consider a six-crystal, tunable, compact cavity [18] as illustrated in figure 1 (the top view is shown in (a) and the side view is shown in (b)). The crystals are arranged in a non-coplanar (3D) scattering geometry. There are two *backscattering* units comprising three crystals (C_1, C_2, and C_3) on one side of the undulator and three crystals (C_4, C_5, and C_6) on the other side. Collimating and focusing elements are shown as $CRL_{1,2}$, which could be grazing-incidence mirrors but are represented in the figure by another possible alternative—compound refractive lenses [37, 38]. In each backscattering unit, three successive Bragg reflections take place from three individual crystals to reverse the direction of the beam from the undulator. Assuming that all the crystals and Bragg reflections are the same, the Bragg angles can be chosen within the range $30° < \theta < 90°$; however, Bragg angles close to $\theta = 45°$ should be avoided to ensure high reflectivity for both linear polarization components, as the reflection plane orientations for each crystal change. The cavity allows for tuning the photon energy in a large spectral range by synchronously changing all Bragg angles. In addition, to ensure constant time of flight, the distance L (which brackets the undulator), and the distance between crystals as characterized by H have to be changed with θ. The lateral size G is kept constant as the resonator is tuned.

Because the C_1C_6 and C_3C_4 lines are fixed, intra-cavity radiation can be out-coupled simultaneously for several users at different places in the cavity, although we only consider out-coupling through C_1 at the present time. Out-coupling through crystals C_1 and C_4 are most favorable, since the direction of the out-coupled beams
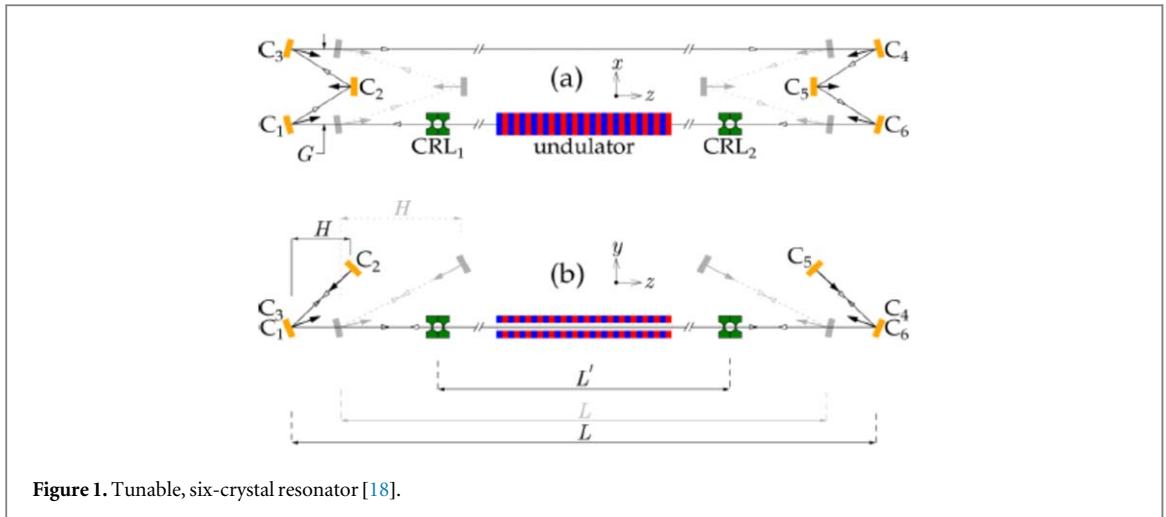
Figure 1. Tunable, six-crystal resonator [18].

do not change with photon energy, but out-coupling for more users through crystals C_3 and C_6 are also possible. Such multi-user capability is in stark contrast with present SASE beamlines which support one user at a time.

We consider that the electron beam propagates from right to left through the undulator and the out-coupling is accomplished through a pinhole in the first downstream mirror (C_1).

3. Rafel simulations

We consider the LCLS-II beamline [20] corresponding to an electron energy of 4.0 GeV, a bunch charge in the range of 10–30 pC with an rms bunch duration (length) at the undulator of 2.0–173 fs (0.6–52 μm) and a repetition rate of 1 MHz. The peak current at the undulator is 1000 A with a normalized emittance of 0.2–0.7 mm mrad, and an rms energy spread of about 125–1500 keV.

We consider the HXR undulator [20] in conjunction with this beamline which is a plane-polarized, hybrid permanent magnet undulator with a variable gap, a period of 2.6 cm, and a peak field of 10 kG. Each HXR undulator has 130 periods, and we consider that the first and last period describe an entry/exit taper. There is a total of 32 segments that can be installed. The break sections between the undulators are 1.0 m in length and contain quadrupoles, BPMs, etc although we only consider the quadrupoles in the simulation which we consider to be located in the center of the breaks. The quadrupoles are assumed to be 7.4 cm in length with a field gradient of 1.71 kG cm^{-1}.

A fundamental resonance at 3.05 keV ($\approx$4.07 Å) implies an undulator field of 5.61 kG. We assume that the electron beam has a normalized emittance of 0.45 mm mrad and a relative energy spread of 1.25 $\times$ 10^{-4}, corresponding to the nominal design specification for the LCLS-II. This yields a Pierce parameter of $\rho \approx 5.4 \times 10^{-4}$. In order to match this beam into the undulator/FODO line, the initial beam size in the x-dimension (y-dimension) is 37.87 μm (31.99 μm) with Twiss $\alpha_x = 1.205$ ($\alpha_y = -0.8656$). Note that this yields Twiss $\beta_x = 24.95$ m and $\beta_y = 17.80$ m.

The resonator dimensions were fixed by means of estimates of the gain using the Ming Xie parameterization [39] and MINERVA simulations that indicated that about 40–60 m of undulator would be required to operate as a RAFEL. As such, we fixed the distance, L, between the two mirrors, C_1 and C_6, framing the undulator as 130 m, which is also the distance separating the two mirrors, C_3 and C_4. In studying the cavity tuning via time-dependent simulations, L allowed to vary while holding fixed the configurations of the *backscattering* units. The compound refractive lenses are placed symmetrically around the undulator and are designed to place the optical focus at the center of the undulator *in vacuo*. In this study, the focal length is approximately 94.5 m.

In order to out-couple the x-rays through a transmissive mirror at the wavelength of interest, the diamond crystal would need to be impractically thin (about 5 μm); hence, we consider out-coupling through a hole in the first downstream mirror. We consider all the mirrors to be 100 μm thick and that the out-coupling of the fundamental is through a hole in the first downstream mirror (C_1). Due to the high computational requirements of time-dependent simulations, we begin with an optimization of the RAFEL with respect to the hole radius and the undulator length using steady-state (i.e. time-independent) simulations.

The choice of hole radius is important because if the hole is too small then the bulk of the power remains within the resonator while if the hole is too large then the losses become too great and the RAFEL cannot lase. The results for the optimization of the hole radius indicate that the optimum hole radius is 135 μm which allows
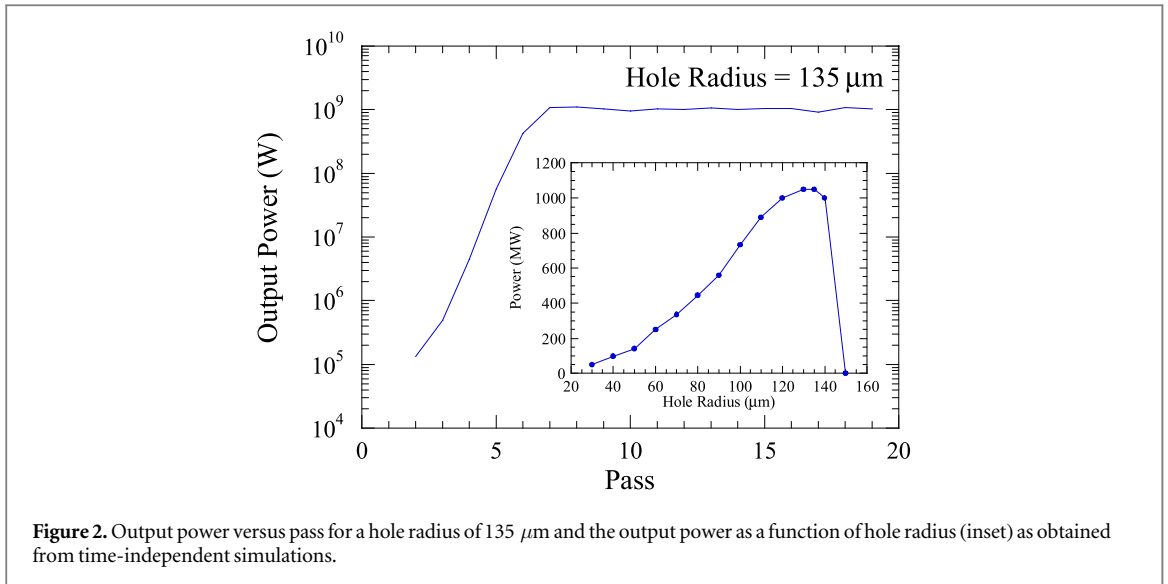
Figure 2. Output power versus pass for a hole radius of 135 μm and the output power as a function of hole radius (inset) as obtained from time-independent simulations.
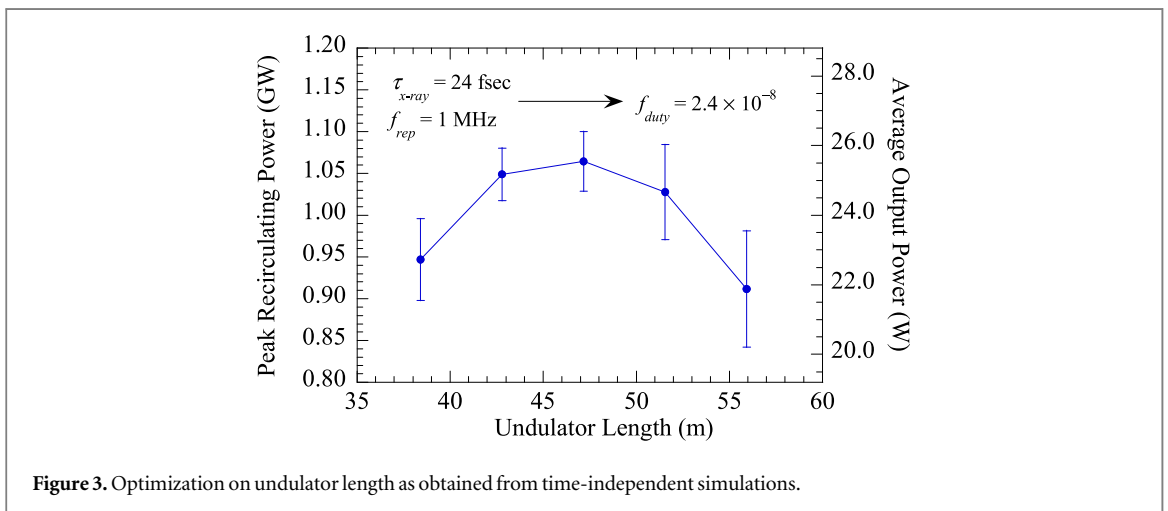

Figure 3. Optimization on undulator length as obtained from time-independent simulations.

for 90% out-coupling, where we fixed the undulator line to consist of 11 HXR undulator segments. This is shown in figure 2 where we plot the output power as a function of pass number for the optimum hole radius and the variation in the saturated power with the hole radius (inset) based upon time-independent simulations.

A local optimization on the undulator length for a hole radius of 135 μm is shown in figure 3 where we plot the peak recirculating power (left axis) and the average output power (right axis), and which is also based upon time-independent simulations. The error bars in the figure indicate the level of pass-to-pass fluctuations in the power which is generally smaller than the level of shot-to-shot fluctuations in SASE. Note that while this represents steady-state simulations, the average power is calculated under the assumption of an electron bunch with a flat-top temporal profile having a duration of 24 fs which yields a duty factor of 2.4×10^{-8}. Each point in the figure refers to a given number of HXR undulators ranging from 9–13 segments. It is evident from the figure that the optimum length is 47.18 m corresponding to 11 segments, as this length both maximizes the average output power and is close to the minimum in the pass-to-pass power fluctuations. Note that while the output power drops quickly when the hole size increases beyond the optimum value (see figure 2), the output power changes more gradual and almost symmetric when the number of undulator segments deviate from the optimum number (see figure 3).

Having optimized the hole radius and the undulator length, we now turn to time-dependent simulations of the RAFEL under the above-mentioned assumption of electron bunches with a flat-top temporal profile having a full width duration of 24 fs and a peak current of 1000 A. This corresponds to a bunch charge of 24 pC. This is within the expected range for the LCLS-II but is not the maximum possible charge; hence, further simulations using a higher charge may yield still higher output power than found here. We further assume an rms energy spread of 0.0125% (the nominal value for the LCLS-II) and take the hole radius in the first downstream mirror (C_1) equal to 135 μm. The simulation was setup to have a bandwidth of 0.8%. We consider start-up from noise
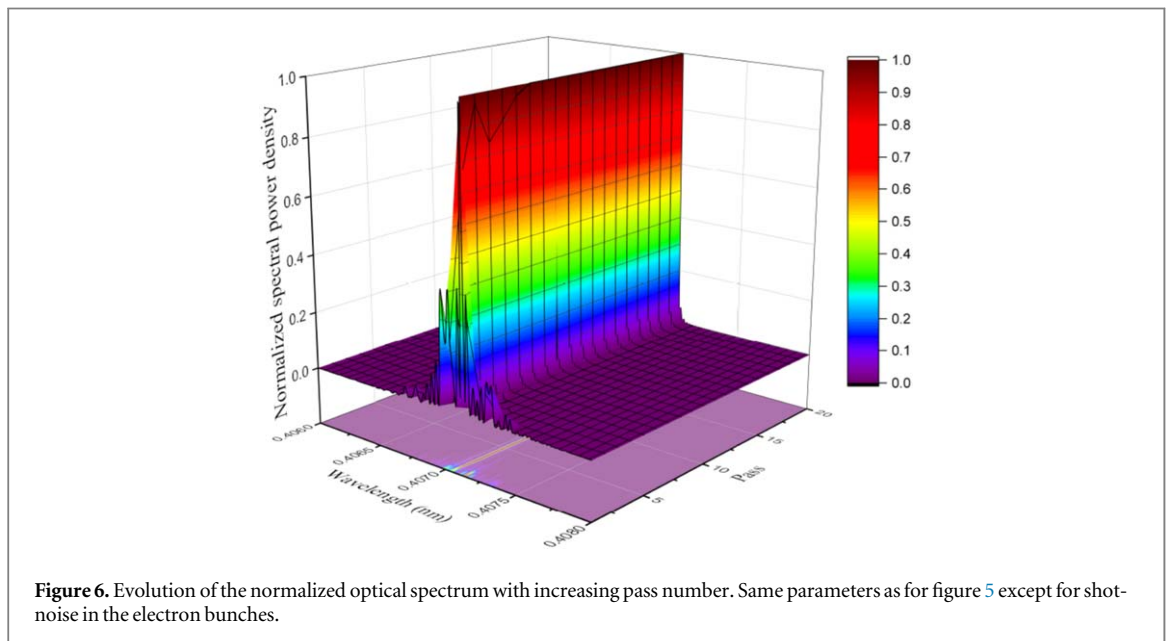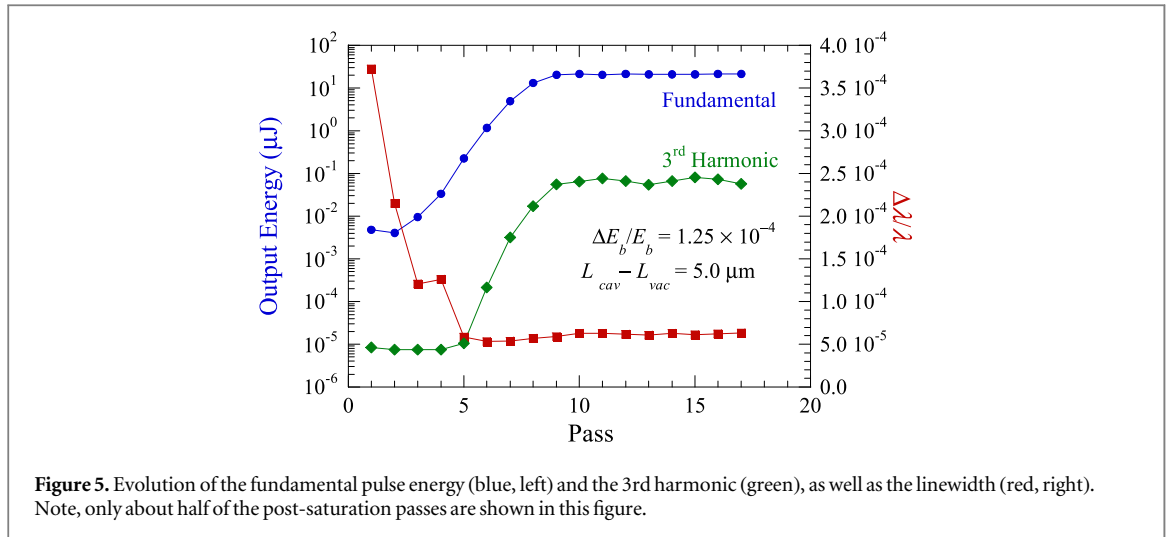
Figure 4. Cavity detuning curve.
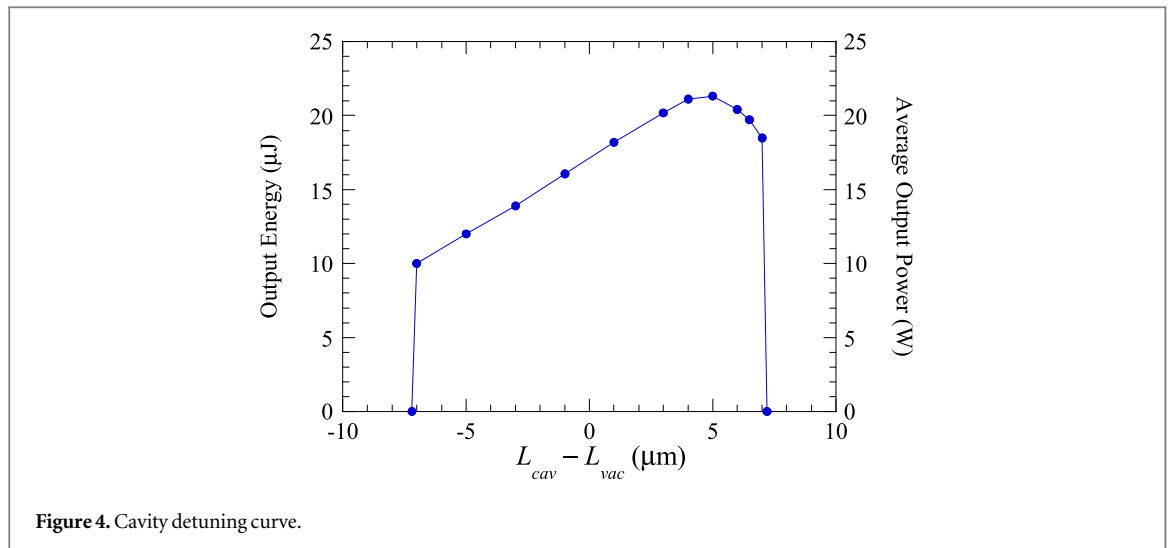
on the electron beam on the first pass (with noise included in the simulations for each successive pass as well) and since the RAFEL employs a high-gain undulator line the pulse energy after the first pass reaches about 5 nJ, and subsequent growth is rapid despite an out-coupling from the first downstream mirror of about 90% of the incident pulse. Typically, saturation is achieved after about 15–25 passes.

The detuning curve defining what cavity lengths are synchronized with the repetition rate of the electrons is shown in figure 4. The synchronous cavity length (the so-called zero-detuning length) is $L_{vac} = c/f_{rep}$, where L_{vac} denotes the synchronous, roundtrip cavity length for the vacuum resonator, f_{rep} is the repetition rate and c is the speed of light *in vacuo*. Here $L_{vac} = 299.792\,4580$ m. As the flat-top temporal profile of an electron bunch corresponds to a bunch length of about 7.2 μm, we expect synchronism for cavity lengths in the range of $L_{vac} - 7.2\ \mu$m $< L_{cav} < L_{vac} + 7.2\ \mu$m, where L_{cav} denotes the total roundtrip length of the cavity. This is indeed observed in figure 4. Once the cavity is detuned by more than the electron bunch length (either positive or negative) the RAFEL fails to lase. As shown in the figure, since the single-pass gain is high in a RAFEL, this transition to complete desynchronization occurs rapidly. It is important to remark that the 'sharp transitions' shown in the figure derive from the high gain combined with our assumption of a flat-top temporal profile. We note that the output pulse energy at the peak of the detuning curve is about 21.2 μJ and the average output power is about 21.2 W for 3.05 keV photons. For an assumed bunch duration of 24 fs and a repetition rate of 1 MHz, this implies that the output power per pulse would be about 880 MW and the long-term average output power is about 21.2 W.

The evolution of the output energy at the fundamental and the 3rd harmonic, and the spectral linewidth of the fundamental, versus pass are shown in figure 5 for a detuning of 5 μm which is close to the peak in the detuning curve (figure 4). While it is not evident in the figure, the rms fluctuation in the energy from pass to pass is about 0.3 μJ ($<$2%), as derived from 14 post saturation passes through the RAFEL. At least as important as the output power is that the linewidth contracts substantially during the exponential growth phase and remains constant through saturation. Starting with a relative linewidth of about 3.7×10^{-4} after the first pass, corresponding to non-saturated SASE, the linewidth contracts to about 6.0×10^{-5} at saturation with a pass-to-pass rms fluctuation of about $\pm$2%. The relative linewidth after the first pass through the undulator is somewhat smaller than the predicted saturated SASE linewidth based on 1D theory [40] which is approximately 5×10^{-4}. Hence, the RAFEL is expected to have both high average power and a stable narrow linewidth.

The 3rd harmonic grows parasitically from high powers/pulse energies at the fundamental in a single pass through the undulator [41] and has been shown to reach output intensities of 0.1% that of the fundamental in a variety of FEL configurations, and this is what we find in the RAFEL simulations. As shown in figure 5, the 3rd harmonic intensity remains small until the fundamental pulse energy reaches about 1 μJ after which it grows rapidly and saturates after about 12 passes. This is close to the point at which the fundamental saturates as well. The saturated pulse energies at the 3rd harmonic reach about 0.067 μJ. Given a repetition rate of 1 MHz, this corresponds to a long-term average power of 67 mW.

A comparison of the performance of the RAFEL with that of an equivalent SASE FEL based upon the same electron beam/undulator/FODO line, which is long enough to reach saturation, shows that the RAFEL exhibits comparable pulse energy and narrower linewidth than the SASE FEL with smaller rms fluctuations. SASE simulations using 15 different noise seeds, which achieves convergence of the average pulse energy to within a few percent, indicates that the average pulse energy is about 22.8 μJ with an rms fluctuation of $\pm$4% which is

Figure 5. Evolution of the fundamental pulse energy (blue, left) and the 3rd harmonic (green), as well as the linewidth (red, right). Note, only about half of the post-saturation passes are shown in this figure.

Figure 6. Evolution of the normalized optical spectrum with increasing pass number. Same parameters as for figure 5 except for shot-noise in the electron bunches.

comparable to the 21.2 μJ found for the RAFEL. However, the average relative linewidth in SASE is about 4.3×10^{-4} with a fluctuation of $\pm 16\%$, which is significantly larger than that found for the RAFEL.

The reduction in the linewidth after saturation shown in figure 5 indicates that a substantial level of longitudinal coherence has been achieved in the saturated regime. The RAFEL starts from shot noise on the beam during the first pass through the undulator. Despite the large roundtrip loss of more than 98%, the optical energy returned to the undulator is still dominant over the noise and longitudinal coherence develops over the subsequent passes. This is depicted in figure 6, which shows the evolution of the normalized optical spectrum with increasing pass number. The optical spectrum is normalized to the maximum spectral power density for each pass to allow easy comparison of the shape of the spectrum. Figure 6 is derived from a second simulation using exactly the same parameters as for figure 5 except for shot-noise in the electron bunches. Both simulations show that the optical field becomes independent of the shot-noise in the electron bunches in less than 5 passes through the RAFEL. Figure 6 shows that only about 3 roundtrips are needed before the optical spectrum condensates into its final shape. That only such a small number of roundtrips are needed is due to the additional spectral filtering by the Bragg mirrors.

Hence, we expect that the temporal profile of the optical field after the first pass will exhibit the typical spiky structure associated with SASE and will strongly depend on the shot-noise in the first electron bunch. Indeed, this is depicted in figures 7 and 8 which shows the temporal profile and associated optical spectrum at the undulator exit after the first pass for the simulation that was used to produce figure 5. Comparing the spectrum shown in figure 8 with the spectrum shown in figure 6 for pass one of the other simulation, we observe the fluctuations expected from the different shot-noise in the electron bunches. The number of temporal spikes
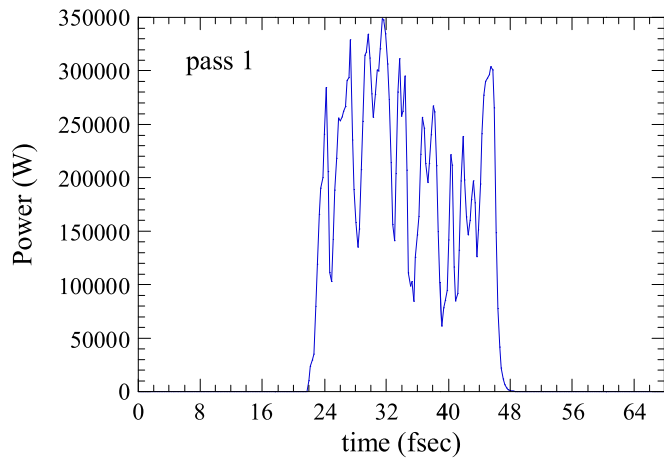
Figure 7. Temporal profile of the optical pulse at the undulator exit after the first pass.
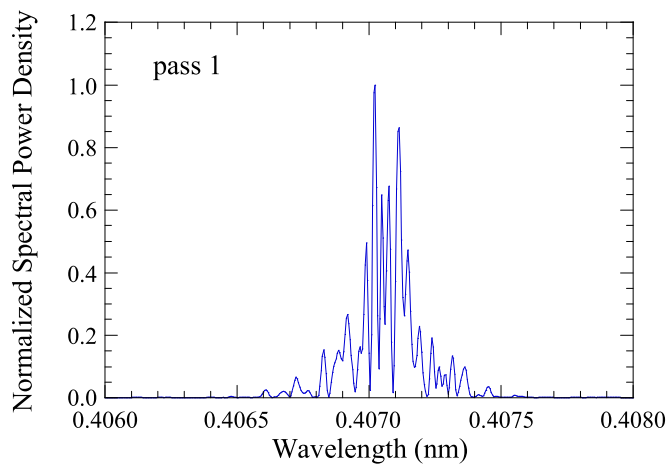

Figure 8. Spectrum at the undulator exit after the first pass for the temporal profile shown in figure 7.

expected for saturated SASE, N_{spikes}, is given approximately by $N_{spikes} \approx l_b/(2\pi l_c)$, where l_b is the rms bunch length and l_c is the coherence length. For the present case, $l_b \approx 7.2$ μm and $l_c \approx 60$ nm; hence, we expect that $N_{spikes} \approx 19$. We observe about 14 spikes in figure 7 which is in reasonable agreement with the expectation. Note that the time axis encompasses the time window used in the simulation.

As indicated in figure 5, the linewidth after the first pass is of the order of 3.7×10^{-4} which is relatively broad and corresponds to the interaction due to SASE. The spectral narrowing that is associated with the development of longitudinal coherence as the interaction approaches saturation (see figure 6) results in a smoothing of the temporal profile. This is illustrated in figure 9, where we plot the temporal profiles of the optical field at the undulator exit corresponding to passes 12–16 which are after saturation has been achieved (left axis). As shown in the figure, the temporal pulse shapes from pass-to-pass are relatively stable and exhibit a smooth plateau with a width of about 23–24 fs which corresponds to, and overlaps, the flat-top profile of the electron bunches which is shown on the right axis. Significantly, the smoothness of the profiles corresponds with the narrow linewidth that results from both having an oscillator configuration as well as the spectral filtering caused by the Bragg mirrors. Both the pass-to-pass stability and smoothness of the output pulses contrast markedly with the large shot-to-shot fluctuations and the spikiness expected from the output pulses in pure SASE.

For clarity, the narrow relative linewidth in this regime of about 7.3×10^{-5} at the undulator exit is shown again in figure 10 after pass 16 and corresponds to the temporal profile shown in figure 9. Such a narrow linewidth as well as the smooth temporal profiles are associated with longitudinal coherence after saturation is achieved.
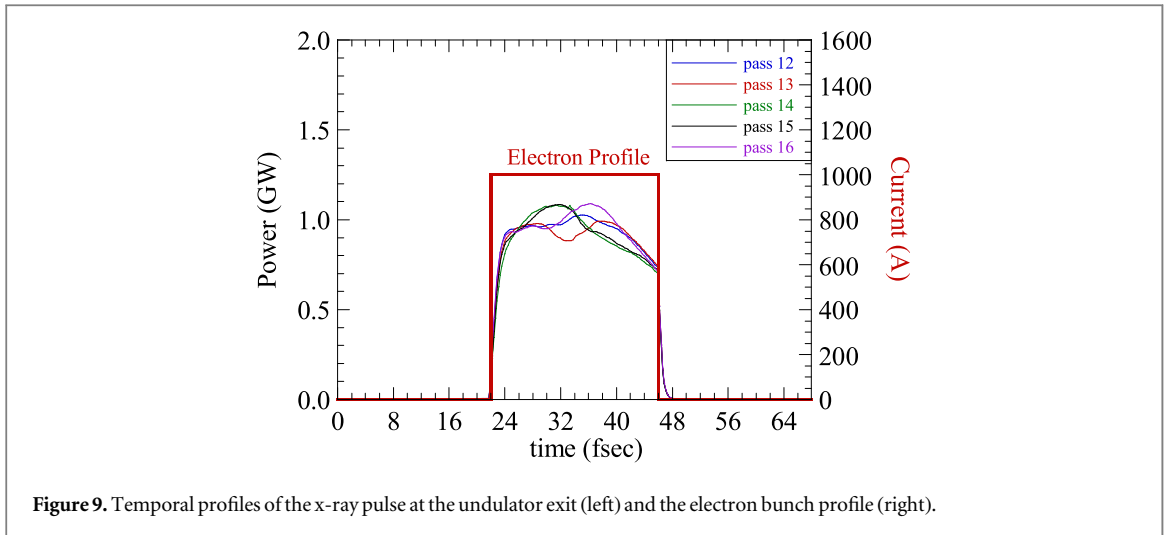
Figure 9. Temporal profiles of the x-ray pulse at the undulator exit (left) and the electron bunch profile (right).
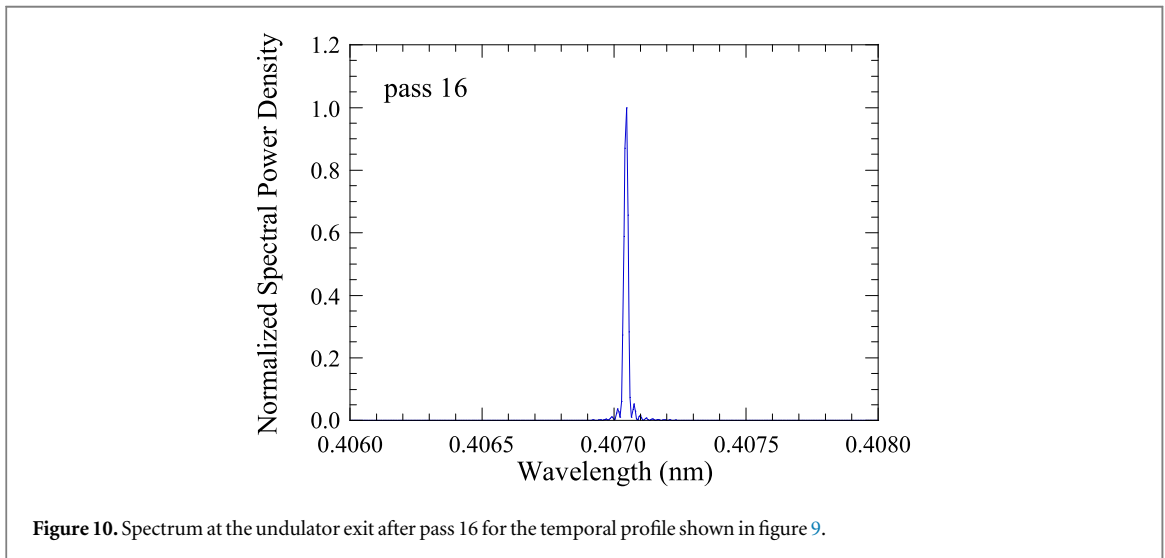

Figure 10. Spectrum at the undulator exit after pass 16 for the temporal profile shown in figure 9.

4. Summary and conclusion

In this paper, we described an x-ray RAFEL using a six-mirror resonator composed of flat diamond crystal Bragg reflectors, one equipped with pinhole out-coupling, that is stabilized with two compound refractive lenses. The advantages of an x-ray RAFEL are demonstrated using nominal LCLS-II-like parameters, i.e. assuming a 4.0 GeV beam with a flat-top temporal pulse profile and the HXR undulator. We studied the generation of 3.05 keV (4.07 Å) x-rays, which were out-coupled through a hole in the first downstream mirror whose optimum radius was found to be 135 μm and through which more than 90% of the x-ray energy was out-coupled. Assuming 24 pC electron bunches and a nominal energy spread of 1.25×10^{-4}, simulations indicate that the peak out-coupled pulse energy was about 21.2 μJ yielding an average output power of 21.2 W. The spectral width was found to decrease markedly with saturation. Third harmonic output was significant reaching average output powers of about 60 mW. It was found that only a few roundtrips ($<$5) were required for fully developed longitudinal coherence, which is mainly due to the spectral filtering of the Bragg mirrors. Further, the output pulse shapes closely correspond to the temporal profile of the electron bunches and are relatively smooth and stable from pass-to-pass.

In comparison with an equivalent saturated SASE FEL, the RAFEL produces comparable pulse energies with a much shorter undulator with a more stable output and narrower linewidth. The fluctuations in the pulse energy in the RAFEL are smaller than that for SASE by more than a factor of two. In addition, the relative linewidth in the RAFEL is smaller than for SASE by a factor of about seven and the fluctuations in the relative linewidth are smaller by a factor of about eight for the system investigated here.

Similar performance is expected for photon energies other than 3.05 keV as the resonator comprised of the Bragg mirrors can be tuned over a large rang of photon energies by appropriate rotation of the Bragg mirrors

while retaining its reflective properties. Using a different temporal profile for the electron bunches would not fundamentally change the characteristics of the x-ray RAFEL. For example, using a parabolic temporal profile in an infrared RAFEL still produces temporally smooth optical pulses [28]. As such, we conclude that an x-ray RAFEL may constitute an important alternative to SASE XFELs.

The present state-of-the-art in the production of diamond crystals provides nearly flawless diamond crystals featuring close to 99% Bragg reflectivity of hard x-rays [16]. A new aspect of the present study is the proposed out-coupling through a pinhole in one of the diamond crystal mirrors. In the present case, we considered a pinhole with a diameter of 270 μm. Diamond is one of the hardest materials and is chemically inert. Mechanical or chemical (including plasma etching) machining techniques are slow and inefficient. An important issue, therefore, is whether diamond mirrors with pinholes can be manufactured with the high crystalline perfection necessary to ensure high Bragg reflectivity.

In our opinion, laser ablation is an appropriate method for the fabrication of pinhole diamond crystal mirrors, and offers a way to control the crystal hole form fidelity. Use of ultra-short (picosecond or femtosecond) laser pulses are essential, as they can mill materials with a small amount of heating and residual damage. The recently demonstrated feasibility of manufacturing diamond parabolic lenses [42, 43] and diamond drumhead crystals [19] by laser milling suggests that this technique could also be successful in its application to the fabrication of diamond pinhole crystal mirrors.

Acknowledgments

References

[1] Emma P *et al* 2009 *Nat. Photon.* **4** 641
[2] Tanaka T *et al* 2012 *Phys. Rev. ST-AB* **15** 110701
[3] Kang H-S *et al* 2017 *Nat. Photon.* **11** 708
    Ko I S *et al* 2017 *Appl. Sci.* **7** 479
[4] Grünert J *et al* 2019 *AIP Conf. Proc.* **2054** 030014
[5] Saldin E L *et al* 2001 *Nucl. Instrum. Methods Phys. Res.* A **475** 357
[6] Amman *et al* 2012 *Nat. Photon.* **6** 693
[7] Kim K-J *et al* 2008 *Phys. Rev. Lett.* **100** 244802
[8] Kim K-J and Shvyd'ko Y 2009 *Phys. Rev. ST-AB* **12** 030703
[9] Lindberg R R and Kim K-J 2009 *Phys. Rev. ST-AB* **12** 070702
[10] Limberg R R *et al* 2011 *Phys. Rev. ST-AB* **14** 010701
[11] Kim K-J *et al* 2012 *Synchrotron Radiat. News* **25** 25
[12] Maxwell T J *et al* 2015 *Proc. Int. Particle Accelerator Conf. (Richmond, Virginia)* p 1897
[13] Kim K-J 2016 A harmonic X-ray FEL oscillator *High-Brightness Sources and Light-Driven Interactions (Long Beach, California)* (*OSA Technical Digest*) (*Long Beach, California, 20-22 March 2016*) p ES2A.2
[14] Qin W *et al* 2017 *Proc. 38th Int. Free-Electron Laser Conf. (Santa Fe, New Mexico)* p 247
[15] Shvyd'ko Y *et al* 2010 *Nat. Phys.* **6** 196
[16] Shvyd'ko Y *et al* 2011 *Nat. Photon.* **5** 539
[17] Stoupin S *et al* 2012 *Phys. Rev.* B **86** 054301
[18] Shvyd'ko Y 2013 Feasibility of x-ray cavities for free-electron laser oscillators *Int. Committee for Future Accelerators: Beam Dynamics Newsletter* ed G R Neil p 68
[19] Kolodziej T *et al* 2016 *J. Appl. Cryst.* **49** 1240
[20] Marcus G *et al* 2014 *Proc. 36th Int. Free-Electron Laser Conf. (Basel, Switzerland)* p 456
[21] Benson S V *et al* 1999 *Nucl. Instrum. Methods Phys. Res.* A **429** 27
[22] Neil G R *et al* 2000 *Phys. Rev. Lett.* **84** 662
[23] Neil G R *et al* 2006 *Nucl. Instrum. Methods Phys. Res.* A **557** 9
[24] Kolodziej T *et al* 2018 *J. Synchrotron Radiat.* **25** 1022
[25] Nguyen D C *et al* 1999 *Nucl. Instrum. Methods Phys. Res.* A **429** 125
[26] Huang Z and Ruth R 2006 *Phys. Rev. Lett.* **96** 144801
[27] McNeil B W J 1990 *IEEE J. Quantum Electron.* **26** 1124
[28] Freund H P *et al* 2013 *Phys. Rev. ST-AB* **16** 010707
[29] Siegman A E 1986 *Lasers* (Sausalito, CA: University Science Books) Ch 20
[30] Freund H P and Antonsen T M Jr 2018 *Principles of Free-Electron Lasers* 3rd edn (Berlin: Springer)
[31] Freund H P *et al* 2017 *New J. Phys.* **19** 023020
[32] Freund H P and van der Slot P J M 2018 *New J. Phys.* **20** 073027
[33] Karssenberg G *et al* 2006 *J. Appl. Phys.* **100** 093106
[34] http://lpno.tnw.utwente.nl/opc.html
[35] Shvyd'ko Y 2004 *X-Ray Optics High-Energy Resolution Applications* (*Optical Sciences*) vol 98 (Berlin: Springer)

[36] van der Slot P J M *et al* 2009 *Phys. Rev. Lett.* **102** 244802

[37] Snigerev A *et al* 1996 *Nature* **384** 49

[38] Lengeler B *et al* 1999 *J. Synchrotron Radiat.* **6** 1153

[39] Xie M 1995 *Proc. 1995 Particle Accelerator Conf.* vol 1 p 183

[40] Huang Z and Kim K-J 2007 *Phys. Rev. ST-AB* **10** 034801

[41] Freund H P *et al* 2001 *J. Quantum Electron.* **37** 790

[42] Terentyev S *et al* 2015 *Appl. Phys. Lett.* **107** 111108

[43] Antipov S *et al* 2016 *J. Synchrotron Radiat.* **23** 163–8